

Co₉S₈ Nanoparticles for Hydrogen Evolution

Jawayria Mujtaba, Le He, Hongqin Zhu, Zhijia Xiao, Gaoshan Huang,* Alexander A. Solovev,* and Yongfeng Mei

Cite This: *ACS Appl. Nano Mater.* 2021, 4, 1776–1785

Read Online

ACCESS |



Metrics & More



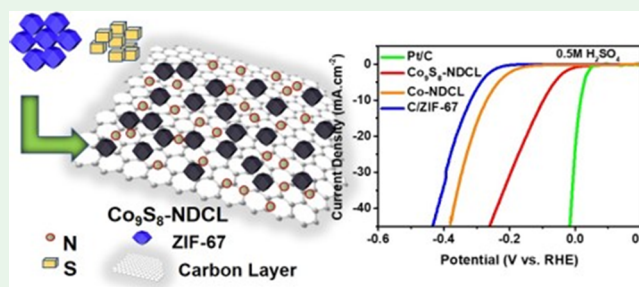
Article Recommendations



Supporting Information

ABSTRACT: The exploration of electrocatalysts for hydrogen evolution, that are stable and efficient in both acidic and alkaline media, is of the momentous importance in the advancement of clean energy production. This paper describes a modest, low-cost, and feasible method to synthesize hierarchical structures of Co₉S₈ nanoparticles cocooned in the N-doped carbon layer (Co₉S₈-NDCL). First, the metal–organic framework, zeolitic imidazolate framework-67, was synthesized and then morphed into Co₉S₈-NDCL nanocomposites by thermal treatment with sulfur powder in an argon environment. The nanocomposite electrocatalyst boosts the efficient functioning in acidic (0.5 M sulfuric acid, H₂SO₄, pH = 0) and basic (1 M potassium hydroxide, KOH, pH = 14) conditions toward the hydrogen evolution reaction (HER). The improved electrocatalytic activity can be ascribed to the hierarchical, porous structure and synergy of Co₉S₈ nanoparticles and the N-doped carbon layer. The Co₉S₈-NDCL nanocomposite electrode attains the current density of 20 mA·cm⁻² for the HER, requiring very low overpotentials of 149 and 219 mV in 0.5 M H₂SO₄ and 1 M KOH aqueous solutions, respectively. It is also observed that the Co₉S₈-NDCL nanocomposites, even after 2000 cycles, exhibited good stability and a small Tafel slope in both media. This study presents a mark in the race of achieving low-cost and highly efficient pristine Co₉S₈ nanocomposites without doping of any precious metals.

KEYWORDS: Co₉S₈, non-Pt catalysts, N-doped carbon, electrocatalysts, hydrogen evolution reaction (HER)



1. INTRODUCTION

The environmental pollution and an urgent need to supersede fossil fuels with clean and sustainable energy is the driving force behind evolving new recyclable energy sources. Hydrogen has become the fore center of the proposed promising chemical fuels for efficient and sustainable energy technologies, owing to its zilch toxic discharges during combustion.¹ Water splitting is a very unpretentious technique to generate hydrogen, although it involves effectual electrocatalysts for the hydrogen evolution reaction (HER) to accomplish a higher current density at low values of overpotential.² Although Pt and other noble metals superlatively enable the reduction of water electrocatalytically into hydrogen, their rareness and high cost diminish their appeal for large-scale applications.³ Hence, much work has been put into developing vastly efficient and stable electrocatalysts for the HER with elements that are plentiful on the earth.⁴

Up to the present time, many non-noble catalysts, for example, transition metal oxides,^{5–7} carbides,^{8,9} selenides,^{8,10,11} nitrides,⁷ phosphides,^{12–14} and sulfides,^{10,15} have been reported for the electrocatalytic reduction of water. Recently, many transition metal sulfides have also been explored as efficient and approvingly active HER catalysts in acidic and basic conditions, considering this as one of the suitable operating conditions of fuel cells and electrolyzers.^{16,17} To

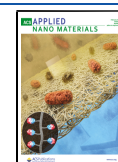
accomplish this, considerable exploration energies have been dedicated to evolving HER catalysts, which are nonprecious metals, stable in a wide pH range and displaying high activities. Among this growing family of HER catalysts, one of the most active members are nanostructured sulfides and other heterostructures of cobalt,^{18–21} nickel,^{22,23} iron,²⁴ molybdenum,²⁵ and tungsten.²⁶

Metal–organic frameworks (MOFs) are composite materials built by linking organic ligands with metal ion clusters. MOFs offer a large specific surface area, along with high porosity, and diverse possibilities of chemical components.^{27–30} Due to these traits, MOFs are known for their unique potential in several applications, including the separation and adsorption of gases,²⁸ drug delivery,³¹ chemical sensors,²⁹ energy storage and conversion,²⁹ and catalysis.³⁰ In recent years, there has been an increase in the use of MOFs as sacrificial templates or precursors to produce porous materials.³² Primarily, various

Received: December 2, 2020

Accepted: January 15, 2021

Published: January 26, 2021



metal oxides and sulfides obtained from MOFs have been presented as notable electrocatalysts.^{33–35} The electrocatalysts derived from the pyrolysis of MOFs have a specific feature of a large surface area, which is responsible for the increased exposure of the active sites and enables the fast charge and mass transport.^{36,37}

The following attributes when present in an electrocatalyst makes it a model candidate for the HER: decent electrical conduction to boost the transfer of electrons,³⁸ nanoscale dimensions for greater active sites that are exposed, morphology with pores to accommodate for the transference of reactants and products,³⁹ and a relatively high width-to-height proportions to enhance the catalytic activity per surface area.⁴⁰ Transition metal sulfides possess good electrical conductivity, which has already been confirmed as advantageous for the electrocatalytic process.^{41,42} Thus, it is convenient to deduce that transition metal sulfides can be a promising candidate for the HER.

In the previous years, cobalt sulfides have already made their mark in the field of energy applications such as supercapacitors, batteries, and overall water splitting.^{43,44} This has been possible due to their good electrical conductivity, outstanding chemical stability, and its natural availability in abundance. But cobalt sulfides have generally performed well when they are combined to form heterostructures with transition metal chalcogenides or there is some metal doping present.^{45–48} The reported studies do not provide enough evidence whether the performance enhancement of heterostructures of cobalt sulfides can exclusively be attributed to it. As most electrodes undergo deterioration in the acidic media, it is important for an electrocatalyst to perform well in an alkaline condition for it to be embraced extensively in the industry.⁴⁹ To the best of our knowledge, till date there are no pristine cobalt sulfides reported, which have performed well in both acidic and alkaline media for the HER.

Herein we report Co₉S₈ nanoparticles cocooned in the N-doped carbon layer (Co₉S₈-NDCL), synthesized by using a feasible, modest, and low-cost method, which employs the sacrificial zeolite imidazole-67 (ZIF-67) as the precursor, which is a conventional MOF. The final product Co₉S₈-NDCL was obtained by the pyrolysis of ZIF-67 with sulfidation in an argon environment. Comparing the Co₉S₈-NDCL with the Co-NDCL (pyrolysis without sulfur powder) and C/ZIF-67 proved that the final products conserved the size uniformity and morphology even after annealing at a high temperature. The cocooning N-doped carbon layer is mesoporous, providing an extra active site to facilitate the catalysis. Henceforth, enhancing the electron transfer and ultimately contributing to achieving lower overpotentials.

The electrocatalytic performance of the as-synthesized nanocomposites was explored, and the Co₉S₈-NDCL displayed an enhanced activity and stability as a catalyst toward the HER in an acidic solution (0.5 M H₂SO₄, pH = 0) as well as in an alkaline solution (1 M KOH, pH = 14). When evaluated as an electrocatalyst for the HER, the Co₉S₈-NDCL reveals an overpotential of 96 mV (0.5 M H₂SO₄) and 146 mV (1 M KOH). The better catalytic activity of the Co₉S₈-NDCL can be owed to its unique structural modification of nanoparticles cocooned in doped mesoporous networks with more exposed active sites.

2. EXPERIMENTAL SECTION

2.1. Materials. Cobalt nitrate hexahydrate (Co(NO₃)₂·6H₂O), 2-methylimidazole, and Nafion were purchased from Aladdin Ltd. (Shanghai, China). The Pt/C (20 wt %) catalyst was purchased from Alfa Aesar. Methanol was obtained from Sinopharm Chemicals, and ethanol was obtained from Titan Ltd. Sulfuric acid (H₂SO₄) (Sigma-Aldrich) and potassium hydroxide (KOH) were purchased from Hushi Corporation (China). All these chemicals were used for the synthesis as received. DI water was used for all experiments.

2.2. Synthesis of ZIF-67. In a typical procedure for the Co₉S₈-NDCL nanocomposite synthesis, first, ZIF-67 was synthesized. A total of 1.16 g of (Co(NO₃)₂·6H₂O) was dissolved in 100 mL of methanol to form a pink solution. Another colorless solution was prepared by adding 1.31 g of 2-methylimidazole in 100 mL of methanol. The colorless solution was swiftly added into a pink solution with constant stirring to get a purple solution. Subsequently, the solution was further aged for a day at room temperature without stirring. The purple powder was then collected by centrifugation, washed with ethanol five times to eradicate all the organic solvents, and dried at 65 °C for 12 h under a vacuum.

2.3. Synthesis of the Co₉S₈-NDCL. To synthesize the Co₉S₈-NDCL, ZIF-67 and sulfur powder were placed in an alumina boat in a 2:1 weight ratio. The furnace was heated to 600 °C and maintained at this temperature for 2 h under an argon gas flow. The black powder obtained after the pyrolysis was washed with ethanol several times and dried at 65 °C for 12 h under a vacuum. The percentage yield of the product obtained is approximately 94%. For comparison, ZIF-67 was annealed for 2 h under the same conditions without sulfur powder to get Co nanoparticles cocooned in the N-doped carbon (Co-NDCL). ZIF-67 was shaken and mixed for 48 h with carbon after being dispersed in ethanol to get C/ZIF-67.

2.4. Characterization. To analyze the phases and crystallinity of the as-synthesized samples, they were characterized by using a Bruker model D8 X-ray diffractometer (XRD) with Cu K α irradiation (λ = 1.5418 Å). Then, the morphological and structural details of the nanocomposites were acquired by using field emission scanning electron microscopy (FESEM, Hitachi-S5500, 5 kV), transmission electron microscopy (TEM, FEI Tecnai G² 20, 200 kV) to further observe, high-resolution transmission electron microscopy (HRTEM, FEI Titan 80–300, 300 kV), X-ray photoelectron spectroscopy (XPS, ESCALAB 250, Al K α), and Raman microscopy (Renishaw, 514.5 nm excitation). To analyze the Brunauer–Emmett–Teller (BET) surface area and pore size, the nitrogen adsorption–desorption isotherm at 77 K was performed using a Micromeritics ASAP 2020 system. Before performing the (N₂) adsorption measurements, the as-prepared sample was degassed at 180 °C. A multipoint BET method was employed to determine the average surface area. The Barrett–Joyner–Halender (BJH) method was used on a desorption isotherm to ascertain the pore size distribution. The thermogravimetric (TG) analysis was performed by using a TGA 2050 thermogravimetric analyzer in the air between the temperature range of 25 and 600 °C (heating rate = 10 °C min⁻¹).

2.5. Electrochemical Measurements. The electrochemical behavior of the products was performed at room temperature, and measurements were made using an electrochemical workstation (CHI 660E). A setup involving three electrodes with a 5 mm diameter glassy carbon electrode (GCE), saturated Ag/AgCl, and a graphite rod was used as the working electrode, reference electrode, and the counter electrode, respectively. The measurements were done in a 0.5 M aqueous solution of H₂SO₄ and 1 M aqueous solution of KOH. The polarization data were collected, and all the potentials stated in this study are reported versus the reversible hydrogen electrode (RHE) by the addition of a factor of “0.197 + 0.059 (pH)”. Linear sweep voltammetry (LSV) was accomplished to determine the HER performance of the nanocomposites at the scan rate of 5 mV s⁻¹, along with rapidly stirring the solution by using a magnetic stir bar. Polarization curves are represented in the graphical form as an overpotential (η) against the logarithm of the current density ($\log j$). This was done to acquire the Tafel curves to quantifying the HER

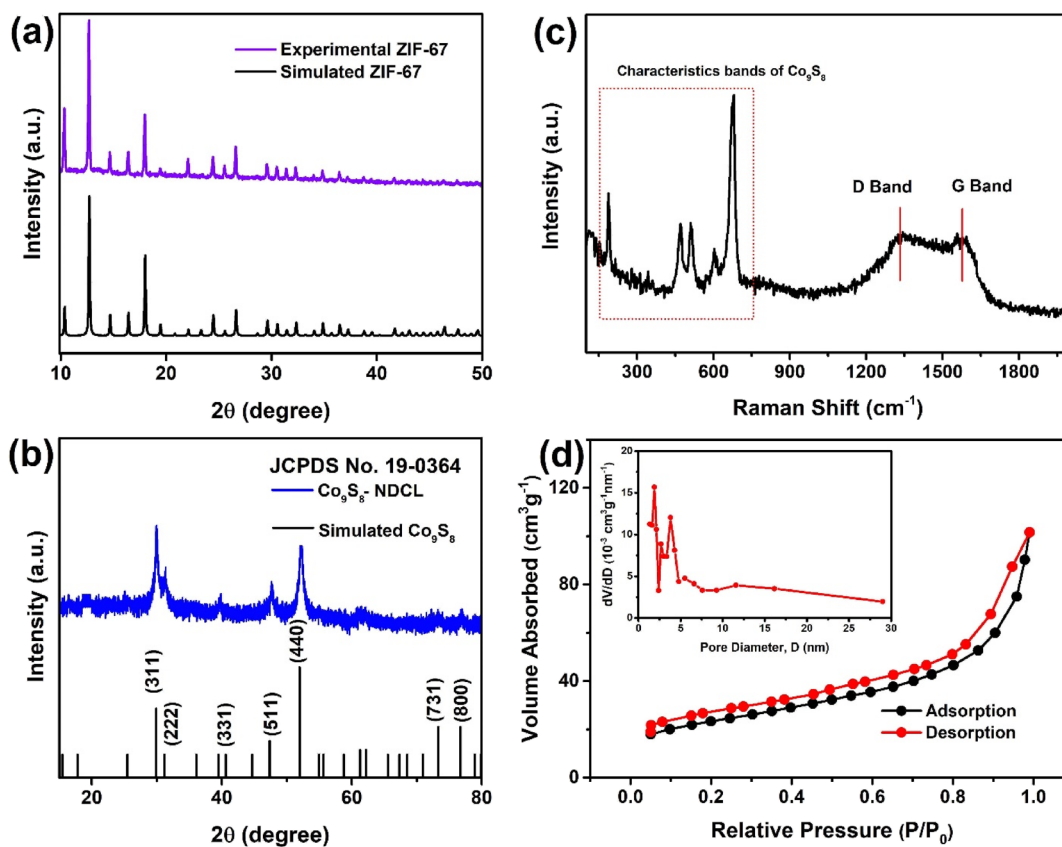
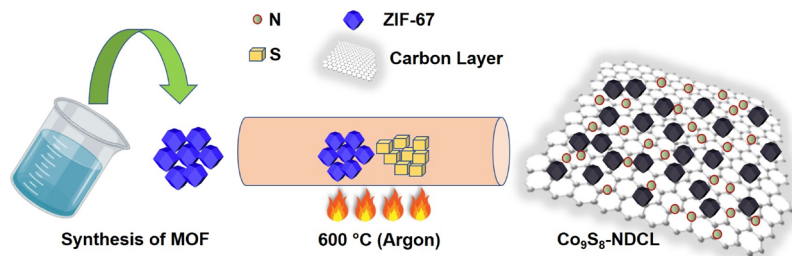
Scheme 1. Schematic Description of the Synthesis Process of the Co₉S₈-NDCL

Figure 1. (a,b) XRD patterns of the as-synthesized and simulated ZIF-67 and Co₉S₈-NDCL, (c) Raman spectrum of Co₉S₈-NDCL, and (d) N₂ adsorption–desorption isotherm and pore size distribution curve (inset) of the Co₉S₈-NDCL.

behaviors of the Co₉S₈-NDCL and ZIF-67. For the calculation of the Tafel slope (b) and deducing the exchange current density (j_0), the linear part of the plotted Tafel curves was fitted to the Tafel equation “($\eta = b \times \log(\frac{j}{j_0})$)”. Moreover, the electrochemical impedance spectroscopy (EIS) has been attained systematically by sweeping the frequency between 10⁵ and 0.1 Hz.

2.6. Preparation of the Working Electrode. At least 3 mg of the as-synthesized catalyst powder (Co₉S₈-NDCL, Co-NDCL, and C/ZIF-67) was added in 1.5 mL of water–isopropyl alcohol (1:0.5 volume ratio) solution with 12.5 μL of Nafion. The obtained mixture of powder and solution was ultrasonicated for a minimum of 60 min to achieve a consistent ink. Then, 20 μL of the prepared mixture was dropped on the GCE, providing a total coverage of approximately 0.2 mg cm⁻². After this, the thinly formed catalyst film was then left to dry in air at an ambient temperature.

3. RESULTS AND DISCUSSION

3.1. Morphology and Structure of the ZIF-67 and Co₉S₈-NDCL. Co₉S₈-NDCL nanocomposites were synthesized

by the pyrolysis of ZIF-67 with sulfur powder in the argon atmosphere (Scheme 1). The structures of Co₉S₈-NDCL and ZIF-67 were determined by the XRD analysis. Figure 1a,b shows the XRD patterns of the ZIF-67 and Co₉S₈-NDCL, respectively. The experimental ZIF-67 peaks are well matched with the simulated data. After the pyrolysis, the peaks corresponding to ZIF-67 disappeared. All of the main diffraction peaks in Figure 1b at 29.9, 31.2, 39.6, 47.6, 52.0, 73.3, and 76.7° could be assigned to the (311), (222), (331), (511), (440), (731), and (800) planes of Co₉S₈, respectively (JCPDS 19-0364).

These observations confirm the successful syntheses of the ZIF-67 and Co₉S₈-NDCL. This can be further verified by the elemental mapping and EDS spectrum of the Co₉S₈-NDCL in Figures S4 and S6, which confirm that Co, S, C, N, and O are present in the as-synthesized nanocomposites. The X-ray diffraction pattern of the Co-NDCL is also provided in Figure S3, which shows that in the absence of sulfur powder during the pyrolysis, there are four prominent peaks which can be

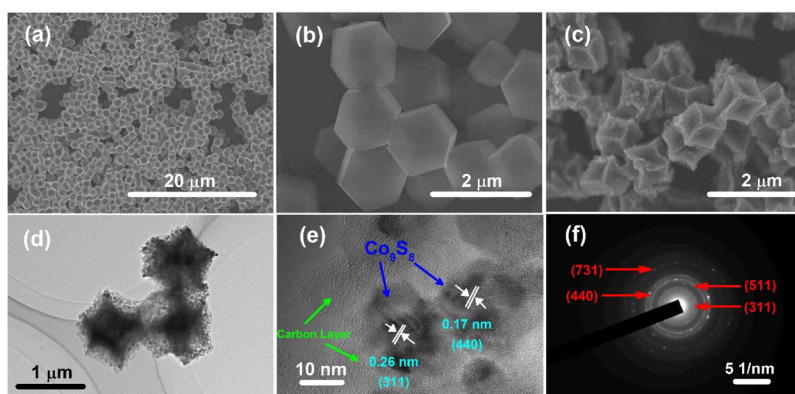


Figure 2. (a,b) FESEM images of ZIF-67, (c) FESEM image of Co_9S_8 -NDCL, (d) TEM image of Co_9S_8 -NDCL, (e) HRTEM image, and (f) SAED pattern of the Co_9S_8 -NDCL.

related with (111), (200), (220), and (311) planes of elementary Co and three peaks, which can be ascribed to the (111), (200), and (220) lattice planes of CoO, indicating the formation of the Co-NDCL. This can be evidenced by the elemental mapping and EDS results in Figures S5 and S7, which validate a large amount of Co and O contents along with N and C.

The phase purity of the synthesized products was confirmed by the lack of any other diffraction peaks from possible impurities. The reasonably high peak intensities of Co_9S_8 indicate that the nanocomposites are highly crystalline. The crystal size (D) of Co_9S_8 nanoparticles can be estimated by using the physical spans of the respective diffraction peak and employing the Debye–Scherrer equation: “ $D = 0.891 \lambda / \beta \cos \theta$ ”, where λ is the wavelength of X-ray, β is the full width at half maximum of the peak, and θ is the Bragg diffraction angle.⁵⁰ The calculated average crystal size by using the (440) peak yielded to be approximately 10.8 nm.⁵¹ Furthermore, this was later confirmed by TEM.

To better understand the nature of the Co_9S_8 -NDCL and also the presence of carbon in the final products, the Raman spectrum was also observed. Figure 1c shows the Raman spectrum for the as-synthesized nanocomposites. The Raman modes observed below and above the 1000 cm^{-1} spectral region can be assigned as characteristic bands of Co_9S_8 and carbon, respectively, and demonstrate that the Co_9S_8 -NDCL is the Co_9S_8 /carbon composite material.^{52–54} Particularly, the peak observed at 1333 cm^{-1} is coherent with the D band, which is a disordered band representing the amorphous carbon and structural defects or edges that can break the symmetry and selection rule, whereas, the peak observed at 1569 cm^{-1} is assigned to the G band, which is associated to the vibration of the sp^2 -hybridized C–C bond of an in-plane hexagonal lattice.⁵² The ratio of the peak intensity of the D band to that of the G band I_D/I_G value is approximately 1, signifying the presence of various defects in the carbon layer, which may be owing to the N-doping. The strong peaks located at 667, 604, 515, 470, and 186 cm^{-1} are characteristic bands of Co_9S_8 .^{55–57} To estimate the amount of the NDCL in the nanocomposites, TG experiments are performed (Figure S10). The initial weight loss at temperatures lower than $200 \text{ }^\circ\text{C}$ can be credited to the elimination of water, whereas the next weight loss, which occurs after approximately $250 \text{ }^\circ\text{C}$, can be attributed to the steady oxidation of the carbon and Co_9S_8 phase in the composites, which produces the weight portion of carbon in the Co_9S_8 -NDCL nanocomposites of approximately

46% as displayed in Figures S10 and S11. The existence of the NDCL in the nanocomposites can intensely boost the electronic conductivity of Co_9S_8 nanoparticles and is also the reason for improving the electrocatalytic performance.

To apprehend the surface area and porous nature of the synthesized hierarchical Co_9S_8 -NDCL, the nitrogen adsorption–desorption isotherm was evaluated. The N_2 adsorption–desorption isotherm at 77 K is shown in Figure 1d. The hysteresis loop for Co_9S_8 -NDCL was observed in the relative pressure range of 0.1–1.0 P/P_0 . The inset in Figure 1d shows the Barrett–Joyner–Halenda (BJH) pore width distribution for the corresponding sample, and the average pore widths were found to be approximately 1.88 and 3.81 nm revealing micro/mesopores in the nanocomposite. The specific surface area was found to be $80.9 \text{ m}^2\text{g}^{-1}$. The surface area of the Co_9S_8 -NDCL is relatively low but still higher than many previously reported Co_9S_8 /carbon composite materials such as carbon-armored Co_9S_8 ($13 \text{ m}^2\text{g}^{-1}$), mesocrystal Co_9S_8 hollow sphere ($52.6 \text{ m}^2\text{g}^{-1}$), and Co_9S_8 ($20.3 \text{ m}^2\text{g}^{-1}$).^{54,58} The specific surface area and porosity play an essential role in the electrocatalytic performance toward the HER.

The FESEM images of the ZIF-67 precursor are shown in Figure 2a,b, revealing homogeneous smooth-surfaced polyhedrons with an average size of $1 \mu\text{m}$. Figure 2c shows that the Co_9S_8 -NDCL nanoparticles are evenly distributed, comparable to the ZIF-67 precursors, inferring that the products even after the pyrolysis have maintained a good size homogeneity and structural morphology similar to that of the ZIF-67 crystals. The surface of the as-prepared particles is coarse and highly porous, which is mainly due to the decomposition of the ZIF-67 and the release of CO_2 and H_2O during the high-temperature treatment. Such structural morphology can be idyllic for the HER because the roughness on the surface of nanoparticles warrants a higher density of active sites, which is valuable with regard to the surface electrochemical reactions as it offers a better catalytic performance, and the N-doped carbon layer can provide passages, and fewer crystal boundaries can help in providing pathways with faster charge transport and less scattering.^{59,60} To further investigate the morphology of the nanocomposites, TEM and HRTEM are performed. Investigating a single large nanoparticle of the Co_9S_8 -NDCL closely, as shown in Figure 2d, the structure is uniformly covered with evenly dispersed Co_9S_8 nanoparticles, which can benefit toward the increasing of the specific surface area of nanocomposites. For over 200 nanoparticles, the statistical analysis was done to estimate the average particle size, which is

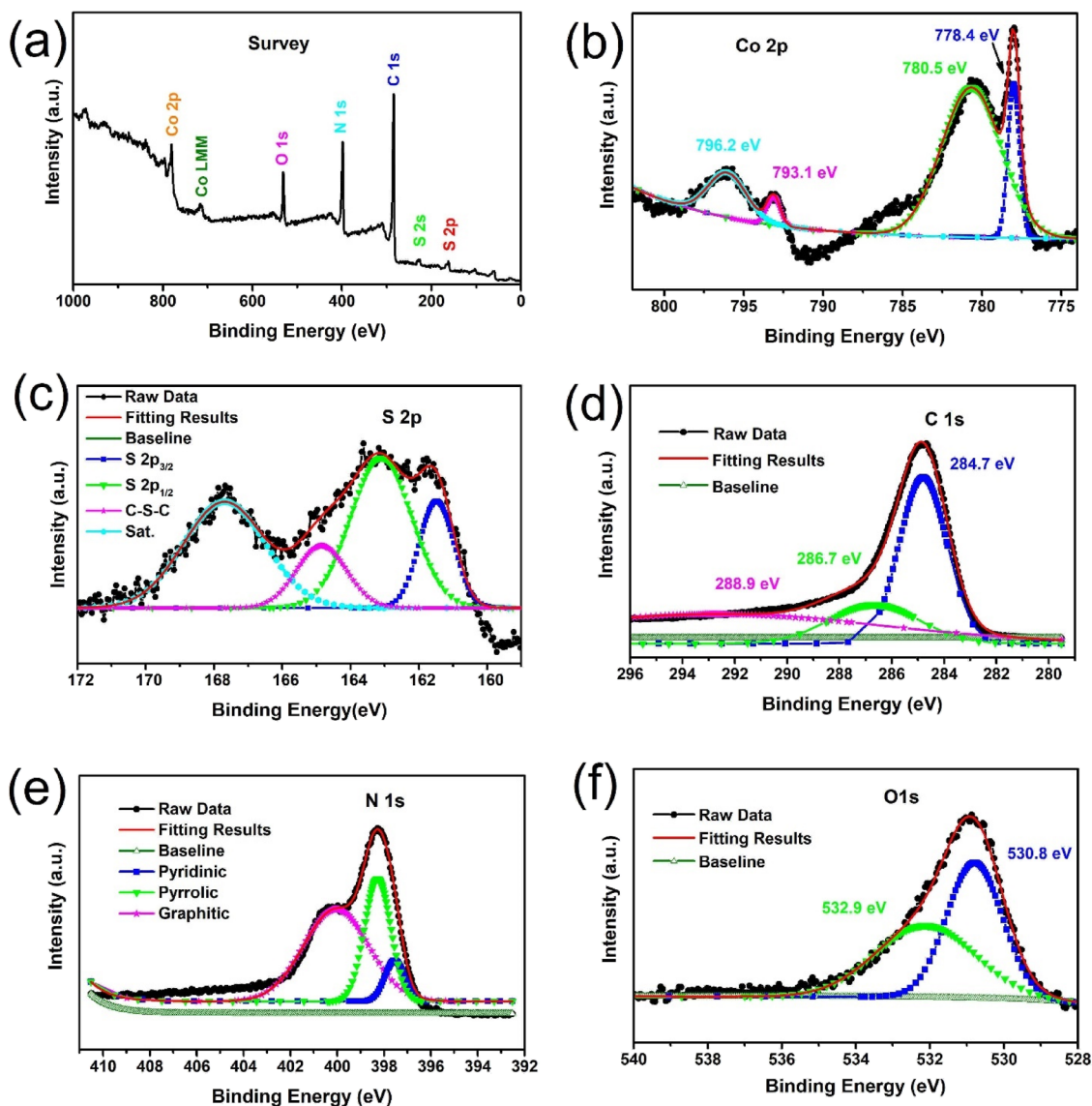


Figure 3. (a) XPS survey spectrum of Co_9S_8 -NDCL. (b–f) High-resolution XPS spectra of Co 2p, S 2p, C 1s, N 1s, and O 1s.

calculated to be approximately 12.2 nm (Figure S1), which supports the XRD results. Several rings presented in the related selected area electron diffraction (SAED) pattern, as exhibited in Figure 2e, can conveniently be indexed to the (311), (511), (440), and (731) planes of the Co_9S_8 . Additionally, the lattice fringes' interplanar distances to be 0.26 and 0.17 nm corresponding to the (311) and (440) planes of Co_9S_8 , respectively, are presented in Figure 2f.

The analysis and the respective XPS spectra for the Co_9S_8 -NDCL to determine the arrangement of electrons and surface chemical composition are presented in Figure 3. The detailed XPS survey is shown in Figure 3a, which constitutes of sulfur, cobalt, carbon, nitrogen, and oxygen. The high-resolution Co 2p displayed in Figure 3b comprises the four major peaks. The two apparent peaks at 778.4 and 793.1 eV are recognized as the Co–S band. Whereas the two other peaks at binding energies of 780.5 and 796.2 eV fit with the Co–O bond.^{61,62} The presence of oxygen in the nanocomposites can be because of the materials' surface oxidation and residual oxygen from the precursor.^{54,63,64}

Furthermore, in the high-resolution S 2p spectrum in Figure 4c, there are two distinct peaks which can be seen at 161.6 and 163.12 eV and are consistent with the previously reported data for the binding energies of $\text{S } 2p_{3/2}$ and $\text{S } 2p_{1/2}$, respectively, accompanied by two other peaks present at 164.88 eV, which belong to C–S–C and 167.7 eV attributed to SO_x ,^{65,66} which further confirm the presence of oxygen.⁶⁷ The C 1s XPS spectrum (Figure 3d) is presented, and the peaks presented at 284.7, 286.7, and 288.9 eV can be related to the binding energies of C–C, C–S/C–N, and C–N bonds, respectively, in the Co_9S_8 -NDCL.^{63,68,69} The prominent peaks in the high-resolution N 1s spectrum (Figure 3e) confirm the existence of nitrogen in the nanocomposites. The peaks centered on the binding energies of 397.4, 398.3, and 400.1 eV can be ascribed to pyridinic, pyrrolic, and graphitic nitrogen, respectively.⁷⁰ This N-doping of the carbon layers in the nanocomposites can boost the conductivity, which is vital in improving the electrocatalyst performance.⁷¹ The high-resolution O 1s spectrum is presented in Figure 3f, and the prominent peak at 532.9 eV is recognized as the binding energy of Co–O, whereas the peak at 530.8 eV can be ascribed to the site of the

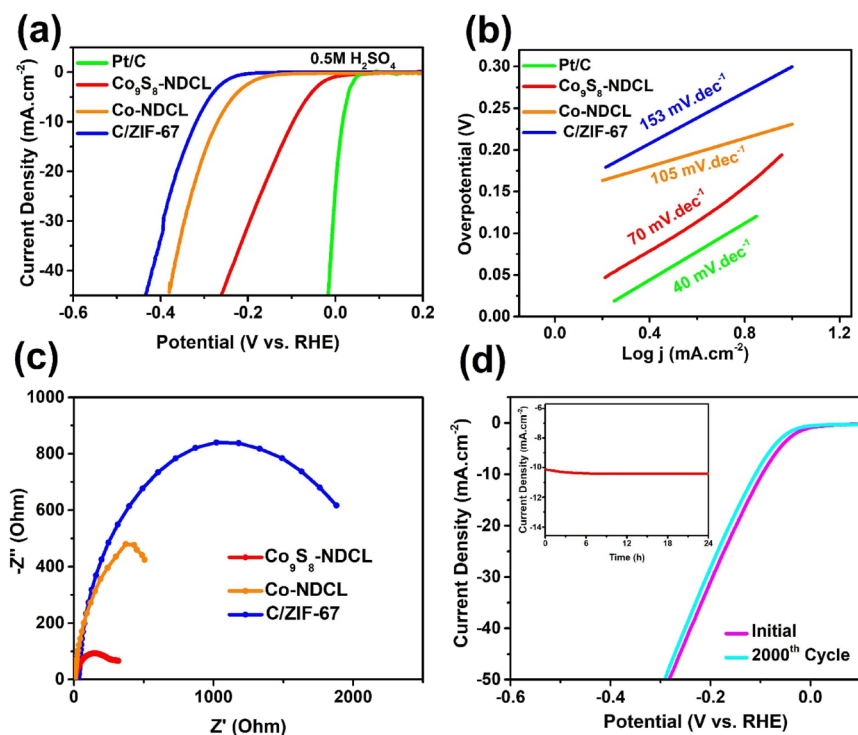


Figure 4. (a) Polarization curves in 0.5 M H_2SO_4 , (b) Tafel curves of Co_9S_8 -NDCL, Co-NDCL C/ZIF-67, and Pt/C, and (c) Nyquist curves of nanomaterials. (d) Stability polarization curves of Co_9S_8 -NDCL in 0.5 M H_2SO_4 initially and after 2000 cycles. The inset shows the durability over 40 h.

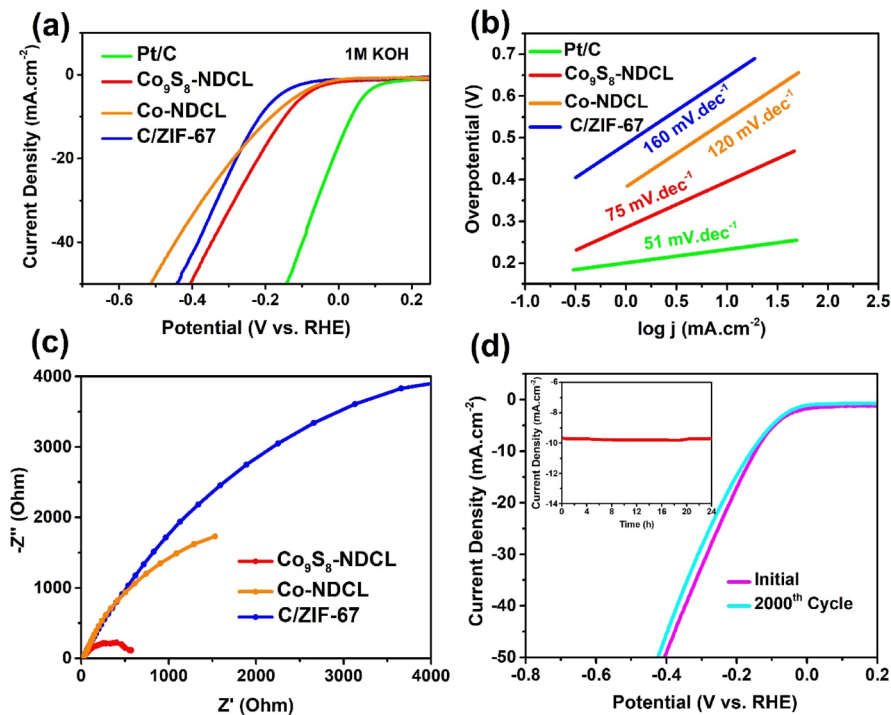


Figure 5. (a) Polarization curves in 1 M KOH, (b) Tafel curves of Co_9S_8 -NDCL, Co-NDCL, C/ZIF-67, and Pt/C. (c) Nyquist curves of nanomaterials. (d) Stability polarization curves of Co_9S_8 -NDCL in 1 M KOH initially and after 2000 cycles, and the inset shows the durability over 24 h.

defect (i.e., oxygen vacancies) in the Co_9S_8 -NDCL, thus, enhancing the material's conductivity and making it active toward the HER.^{72,73}

3.2. Electrocatalytic Performance of the Co_9S_8 -NDCL.

To study the activity of the Co_9S_8 -NDCL as a HER catalyst,

the as-prepared catalysts inks were laden on a GCE to inspect the cyclic voltammetry (CV) performance in an argon-saturated 0.5 M H_2SO_4 (Figure 4). The linear sweep voltammogram (LSV) measurements were done, as shown in Figure 4a. As investigated, all the nanomaterials show an onset

overpotential of 51 mV. The Co₉S₈-NDCL, Co-NDCL, and C/ZIF-67 require overpotentials of 96, 268, and 318 mV, respectively, at the current density of 10 mA·cm⁻². The Pt/C was also evaluated and showed the lowest values of overpotential.

Meanwhile, as displayed in Figure 4b, the Tafel slope displayed for Co₉S₈-NDCL was calculated to be as small as 70 mV dec⁻¹, whereas the Co-NDCL and C/ZIF-67 exhibit somewhat higher Tafel slopes of 105 and 153 mV dec⁻¹, respectively. The Co₉S₈-NDCL presents a higher exchange current density (j_0) when the intersection between the extrapolated linear portion of Tafel curves with the x axis are calculated. It was found to be 0.516 mA cm⁻². As it is well known in discussing the electrode reaction, j_0 , is an intrinsic property, depending only on the material used as a catalyst, the electrolyte used, and the temperature at which catalysis is performed. It suggests the ease and hindrance with which electron is transferred and hence reveals the nuisance in an electrode reaction. The higher value of j_0 can be attributed to the faster HER kinetics for the Co₉S₈-NDCL. The electrochemical active surface area (ECSA) is another noteworthy parameter for assessing the efficiency of the HER electrocatalyst. The ECSA was calculated by estimating the electrochemical double-layer capacitance (C_{dl} , linearly proportional to the ESCA), which was reached through the cyclic voltammetry (CV) measurement. The CV curves of the Co₉S₈-NDCL at different scan rates (10–90 mV s⁻¹) in the potential range from 0.44 to 0.54 V is presented in Figure S13. The C_{dl} value, which is the slope of linear fitting of the CV curves, reveals that the Co₉S₈-NDCL have a $C_{dl} = 10.61$ mF·cm⁻², indicating more active sites.

Moreover, the EIS was also achieved in order to foster the electrocatalytic activity of the Co₉S₈-NDCL nanocomposites. The Nyquist plots of the as-synthesized nanocomposites were accomplished, and the used circuit model is $R_s (R_{ct} \text{ CPE})$. As presented in Figure 4c, the Nyquist plot resulting from the EIS of the Co₉S₈-NDCL is displayed as a well-defined semicircle, the diameter of which corresponds to reaction resistances (R_{ct}).^{74,75} The Co₉S₈-NDCL demonstrates that the charge resistance is lower which in turn supports for a higher rate of charge transfer and swift catalytic kinetics. Figure 4d displays the polarization curves of the Co₉S₈-NDCL in 0.5 M H₂SO₄ initially and after 2000 cycles. To understand the change in morphology of the Co₉S₈-NDCL after stability testing (2000 cycles), the sample is inspected using SEM and TEM (Figure S12). It is noticeable that the size and morphology of the Co₉S₈-NDCL are nearly the same as in the original form, signifying the decent structural and morphological cyclability.

Similarly, the performance in an argon-saturated 1 M KOH solution is presented in Figure 5, where the synthesized Co₉S₈-NDCL nanocomposite displayed an overpotential of 146 mV (Co-NDCL = 184, C/ZIF-67 = 218 mV), with a Tafel slope of 51 mV dec⁻¹, proving a fast current response rate in an alkaline solution (Figure 5a,b). Figure 5c,d exhibits the Nyquist and stability graphs, which show no noticeable degradation in the performance of the electrode even after 24 h. These results are a positive outcome for the Co₉S₈-NDCL nanocomposites to be used in a wide pH range HER.

All the abovementioned interpretations of the electrocatalytic behavior of the Co₉S₈-NDCL indicate that it is better as compared to other previously reported nanomaterials synthesized by the pyrolysis of ZIF-67. When analyzed and tested, for the HER, the Co₉S₈-NDCL reveals a superior catalytic activity

and stability, and this could be accredited to the following explanations: (1) the Co₉S₈-NDCL has a larger active surface area (Figure 1d) because of its porous and matrixed morphology, which allows for the increased interaction between an electrocatalyst/electrolyte and by employing these active sites, leading to an enhanced catalytic performance. (2) Nyquist plots in both acidic and alkaline media possess a smaller diameter, indicating the lower resistance offered during the charge transfer, and hence speeding up the electrode kinetics. All the electrochemical activity details are tabulated in Tables S1 and S3. The comparison of the Co₉S₈-NDCL in the acidic and alkaline electrolytes is presented in Figure S8.

4. CONCLUSIONS

In a nutshell, the MOF-derived Co₉S₈-NDCL hierarchical nanocomposites with unique morphology, including nanoparticles and N-doped carbon layers, were successfully synthesized by using a facile method using ZIF-67 as the precursor. Electrochemical testing reveals that the Co₉S₈-NDCL is a better electrocatalyst toward the HER in acidic and alkaline solutions, with an efficient activity and better stability. This work provides a practical and facile method for preparing transition metal sulfides as catalysts for the hydrogen evolution reaction, which help develop the non-Pt catalysts.

■ ASSOCIATED CONTENT

Supporting Information

The Supporting Information is available free of charge at <https://pubs.acs.org/doi/10.1021/acsnm.0c03171>.

Additional SEM and TEM images, comparison of overpotentials of the as-prepared catalysts, details of the HER activity, TGA and DTA curves, XRD patterns of the TGA experiment products, EDS, CV curves, and comparison with previously reported works (PDF)

■ AUTHOR INFORMATION

Corresponding Authors

Gaoshan Huang – Department of Materials Science, Fudan University, Shanghai 200433, China; orcid.org/0000-0002-0525-7177; Email: gshuang@fudan.edu.cn

Alexander A. Solovev – Department of Materials Science, Fudan University, Shanghai 200433, China; orcid.org/0000-0001-5918-3102; Email: solovevlab@gmail.com

Authors

Jawayria Mujtaba – Department of Materials Science, Fudan University, Shanghai 200433, China

Le He – Functional Nano & Soft Materials Laboratory, Soochow University, Suzhou 215123, P. R. China; orcid.org/0000-0002-4520-0482

Hongqin Zhu – Department of Materials Science, Fudan University, Shanghai 200433, China

Zhijia Xiao – Department of Materials Science, Fudan University, Shanghai 200433, China

Yongfeng Mei – Department of Materials Science, Fudan University, Shanghai 200433, China; orcid.org/0000-0002-3314-6108

Complete contact information is available at: <https://pubs.acs.org/doi/10.1021/acsnm.0c03171>

Notes

The authors declare no competing financial interest. All authors have given approval to the final version of the manuscript.

ACKNOWLEDGMENTS

The authors thank the financial support from the National Natural Science Foundation of China grants (nos. 51602056, 51961145108, U1632115, and 51475093), Science and Technology Commission of Shanghai Municipality (17JC1401700), the National Key Technologies R&D Program of China (2015ZX02102-003), the Program of Shanghai Academic Research Leader (19XD1400600), BRICS, and the Changjiang Young Scholars Program of China. J.M. would like to dedicate this work to her beloved father who passed away in November, 2020.

REFERENCES

- (1) Hunter, B. M.; Blakemore, J. D.; Deimund, M.; Gray, H. B.; Winkler, J. R.; Müller, A. M. Highly Active Mixed-Metal Nanosheet Water Oxidation Catalysts Made by Pulsed-Laser Ablation in Liquids. *J. Am. Chem. Soc.* **2014**, *136*, 13118–13121.
- (2) Walter, M. G.; Warren, E. L.; McKone, J. R.; Boettcher, S. W.; Mi, Q.; Santori, E. A.; Lewis, N. S. Solar Water Splitting Cells. *Chem. Rev.* **2010**, *110*, 6446–6473.
- (3) Gray, H. B. Powering the planet with solar fuel. *Nat. Chem.* **2009**, *1*, 7.
- (4) Xiao, P.; Chen, W.; Wang, X. A Review of Phosphide-Based Materials for Electrocatalytic Hydrogen Evolution. *Adv. Energy Mater.* **2015**, *5*, 1500985.
- (5) Zhu, Y. P.; Ma, T. Y.; Jaroniec, M.; Qiao, S. Z. Self-Templating Synthesis of Hollow Co₃O₄ Microtube Arrays for Highly Efficient Water Electrolysis. *Angew. Chem., Int. Ed.* **2017**, *56*, 1324–1328.
- (6) Gong, M.; Zhou, W.; Tsai, M. C.; Zhou, J.; Guan, M.; Lin, M. C.; Zhang, B.; Hu, Y.; Wang, D. Y.; Yang, J.; Pennycook, S. J.; Hwang, B. J.; Dai, H. Nanoscale nickel oxide/nickel heterostructures for active hydrogen evolution electrocatalysis. *Nat. Commun.* **2014**, *5*, 4695.
- (7) Chen, W. F.; Sasaki, K.; Ma, C.; Frenkel, A. I.; Marinkovic, N.; Muckerman, J. T.; Zhu, Y.; Adzic, R. R. Hydrogen-evolution catalysts based on non-noble metal nickel-molybdenum nitride nanosheets. *Angew. Chem., Int. Ed.* **2012**, *51*, 6131–6135.
- (8) Murthy, A. P.; Theerthagiri, J.; Madhavan, J.; Murugan, K. Enhancement of hydrogen evolution activities of low-cost transition metal electrocatalysts in near-neutral strongly buffered aerobic media. *Electrochem. Commun.* **2017**, *83*, 6–10.
- (9) Li, F.; Zhao, X.; Mahmood, J.; Okyay, M. S.; Jung, S. M.; Ahmad, I.; Kim, S. J.; Han, G. F.; Park, N.; Baek, J. B. Macroporous Inverse Opal-like Mo₂C with Incorporated Mo Vacancies for Significantly Enhanced Hydrogen Evolution. *ACS Nano* **2017**, *11*, 7527–7533.
- (10) Ambrosi, A.; Sofer, Z.; Pumera, M. 2H → 1T phase transition and hydrogen evolution activity of MoS₂, MoSe₂, WS₂ and WSe₂ strongly depends on the MX₂ composition. *Chem. Commun.* **2015**, *51*, 8450–8453.
- (11) Tang, H.; Dou, K.; Kaun, C.-C.; Kuang, Q.; Yang, S. MoSe₂ nanosheets and their graphene hybrids: synthesis, characterization and hydrogen evolution reaction studies. *J. Mater. Chem. A* **2014**, *2*, 360–364.
- (12) Gao, Y.; Lang, Z.; Yu, F.; Tan, H.; Yan, G.; Wang, Y.; Ma, Y.; Li, Y. A Co₂P/WC Nano-Heterojunction Covered with N-Doped Carbon as Highly Efficient Electrocatalyst for Hydrogen Evolution Reaction. *ChemSusChem* **2018**, *11*, 1082–1091.
- (13) Zhang, X.; An, L.; Yin, J.; Xi, P.; Zheng, Z.; Du, Y. Effective Construction of High-quality Iron Oxy-hydroxides and Co-doped Iron Oxy-hydroxides Nanostructures: Towards the Promising Oxygen Evolution Reaction Application. *Sci. Rep.* **2017**, *7*, 43590.
- (14) Xu, Y.; Wu, R.; Zhang, J.; Shi, Y.; Zhang, B. Anion-exchange synthesis of nanoporous FeP nanosheets as electrocatalysts for hydrogen evolution reaction. *Chem. Commun.* **2013**, *49*, 6656–6658.
- (15) Zhao, X.; Ma, X.; Sun, J.; Li, D.; Yang, X. Enhanced Catalytic Activities of Surfactant-Assisted Exfoliated WS₂ Nanodots for Hydrogen Evolution. *ACS Nano* **2016**, *10*, 2159–2166.
- (16) Li, H.; Li, T.-T.; Qian, J.; Mei, Y.; Zheng, Y.-Q. CuCo₂S₄ integrated multiwalled carbon nanotube as high-performance electrocatalyst for electroreduction of nitrogen to ammonia. *Int. J. Hydrogen Energy* **2020**, *45*, 14640–14647.
- (17) Mei, Y.; Li, T.-T.; Qian, J.; Li, H.; Wu, M.; Zheng, Y.-Q. Construction of a C@MoS₂@C sandwiched heterostructure for accelerating the pH-universal hydrogen evolution reaction. *Chem. Commun.* **2020**, *56*, 13393–13396.
- (18) Karuppasamy, K.; Bose, R.; Jothi, V. R.; Vikraman, D.; Jeong, Y.-T.; Arunkumar, P.; Velusamy, D. B.; Maiyalagan, T.; Alfantazi, A.; Kim, H.-S. High performance, 3D-hierarchical CoS₂/CoSe@C nanohybrid as an efficient electrocatalyst for hydrogen evolution reaction. *J. Alloys Compd.* **2020**, *838*, 155537.
- (19) Ehsan, M. A.; Khalafallah, D.; Zhi, M.; Hong, Z. Synthesis of Au/Co₉S₈ composite aerogels by one-step sol-gel method as hydrogen evolution reaction electrocatalysts. *J. Porous Mater.* **2020**, *278*.
- (20) Kim, M.; Anjum, M. A. R.; Choi, M.; Jeong, H. Y.; Choi, S. H.; Park, N.; Lee, J. S. Covalent 0D–2D Heterostructuring of Co₉S₈–MoS₂ for Enhanced Hydrogen Evolution in All pH Electrolytes. *Adv. Funct. Mater.* **2020**, *30*, 2002536.
- (21) Zhao, Z.; Zhang, Z.; Zhao, Y.; Liu, J.; Liu, C.; Wang, Z.; Zheng, G.; Huang, G.; Mei, Y. Atomic Layer Deposition Inducing Integration of Co, N Codoped Carbon Sphere on 3D Foam with Hierarchically Porous Structures for Flexible Hydrogen Producing Device. *Adv. Funct. Mater.* **2019**, *29*, 1906365.
- (22) Li, X.; Wang, X. H.; Zhang, R.; Chen, G.; Zhang, Y.; Chen, D.; Zhang, C.; Zhang, J.; Tan, Y.; Li, B. L.; Luo, H. Q.; Li, N. B. Triggering water splitting to hydrogen and oxygen by phase chemistry in nanoscale nickel electrocatalysts. *J. Alloys Compd.* **2020**, *843*, 156011.
- (23) Zhang, Z.; Deng, L.; Zhao, Z.; Zhao, Y.; Yang, J.; Jiang, J.; Huang, G.; Mei, Y. Nickel nanograins anchored on a carbon framework for an efficient hydrogen evolution electrocatalyst and a flexible electrode. *J. Mater. Chem. A* **2020**, *8*, 3499–3508.
- (24) Zheng, D.; Jing, Z.; Zhao, Q.; Kim, Y.; Li, P.; Xu, H.; Li, Z.; Lin, J. Efficient Co-doped pyrrhotite Fe_{0.9}SS_{1.05} nanoplates for electrochemical water splitting. *Chem. Eng. J.* **2020**, *402*, 125069.
- (25) Zhao, J.; Zhang, D.; Guo, F.; Guo, H.; Liu, Y.; Yin, Y.; Hu, H.; Wang, X. Facile one-pot supercritical synthesis of MoS₂/pristine graphene nanohybrid as a highly active advanced electrocatalyst for hydrogen evolution reaction. *Appl. Surf. Sci.* **2020**, *531*, 147282.
- (26) Hussain, S. R. I.; Vikraman, D.; Feroze, A.; Ali, M.; Seo, Y.-S.; Kim, H.-S.; Chun, S.-H.; Jung, J. One-Pot Synthesis of W₂C/WS₂ Hybrid Nanostructures for Improved Hydrogen Evolution Reactions and Supercapacitors. *Nanomaterials* **2020**, *10*, 1597.
- (27) Eddaoudi, M.; Kim, J.; Rosi, N.; Vodak, D.; Wachter, J.; O’Keeffe, M.; Yaghi, O. M. Systematic Design of Pore Size and Functionality in Isoreticular MOFs and Their Application in Methane Storage. *Science* **2002**, *295*, 469–472.
- (28) Zhao, Z.; Ma, X.; Kasik, A.; Li, Z.; Lin, Y. S. Gas Separation Properties of Metal Organic Framework (MOF-5) Membranes. *Ind. Eng. Chem. Res.* **2013**, *52*, 1102–1108.
- (29) Stassen, I.; Burtch, N.; Talin, A.; Falcaro, P.; Allendorf, M.; Ameloot, R. An updated roadmap for the integration of metal-organic frameworks with electronic devices and chemical sensors. *Chem. Soc. Rev.* **2017**, *46*, 3185–3241.
- (30) Farrusseng, D.; Aguado, S.; Pinel, C. Metal–Organic Frameworks: Opportunities for Catalysis. *Angew. Chem., Int. Ed.* **2009**, *48*, 7502–7513.
- (31) Cai, W.; Chu, C.-C.; Liu, G.; Wang, Y.-X. J. Metal–Organic Framework-Based Nanomedicine Platforms for Drug Delivery and Molecular Imaging. *Small* **2015**, *11*, 4806–4822.

- (32) Zhang, X.; Liu, S.; Zang, Y.; Liu, R.; Liu, G.; Wang, G.; Zhang, Y.; Zhang, H.; Zhao, H. Co/Co₉S₈@S,N-doped porous graphene sheets derived from S, N dual organic ligands assembled Co-MOFs as superior electrocatalysts for full water splitting in alkaline media. *Nano Energy* **2016**, *30*, 93–102.
- (33) Liu, T.; Li, P.; Yao, N.; Cheng, G.; Chen, S.; Luo, W.; Yin, Y. CoP-Doped MOF-Based Electrocatalyst for pH-Universal Hydrogen Evolution Reaction. *Angew. Chem., Int. Ed.* **2019**, *58*, 4679–4684.
- (34) Tan, T.; Tao, P.; Li, X.; Imhanria, S.; Deng, J.; Wang, W. Nitrogen-modified metal-organic framework-based carbon: An effective non-precious electrocatalyst for oxygen reduction reaction. *Catal. Commun.* **2020**, *146*, 106135.
- (35) Thangasamy, P.; Shanmuganathan, S.; Subramanian, V. A NiCo-MOF nanosheet array based electrocatalyst for the oxygen evolution reaction. *Nanoscale Adv.* **2020**, *2*, 2073–2079.
- (36) Wang, H.-F.; Chen, L.; Pang, H.; Kaskel, S.; Xu, Q. MOF-derived electrocatalysts for oxygen reduction, oxygen evolution and hydrogen evolution reactions. *Chem. Soc. Rev.* **2020**, *49*, 1414–1448.
- (37) Zhu, Q.-L.; Xia, W.; Akita, T.; Zou, R.; Xu, Q. Metal-Organic Framework-Derived Honeycomb-Like Open Porous Nanostructures as Precious-Metal-Free Catalysts for Highly Efficient Oxygen Electroreduction. *Adv. Mater.* **2016**, *28*, 6391–6398.
- (38) Lukowski, M. A.; Daniel, A. S.; Meng, F.; Forticaux, A.; Li, L.; Jin, S. Enhanced Hydrogen Evolution Catalysis from Chemically Exfoliated Metallic MoS₂ Nanosheets. *J. Am. Chem. Soc.* **2013**, *135*, 10274–10277.
- (39) Kibsgaard, J.; Chen, Z.; Reinecke, B. N.; Jaramillo, T. F. Engineering the surface structure of MoS₂ to preferentially expose active edge sites for electrocatalysis. *Nat. Mater.* **2012**, *11*, 963.
- (40) Chen, Z.; Cummins, D.; Reinecke, B. N.; Clark, E.; Sunkara, M. K.; Jaramillo, T. F. Core-shell MoO₃-MoS₂ Nanowires for Hydrogen Evolution: A Functional Design for Electrocatalytic Materials. *Nano Lett.* **2011**, *11*, 4168–4175.
- (41) Sun, Y.; Zhang, T.; Li, C.; Xu, K.; Li, Y. Compositional engineering of sulfides, phosphides, carbides, nitrides, oxides, and hydroxides for water splitting. *J. Mater. Chem. A* **2020**, *8*, 13415–13436.
- (42) Zahra, R.; Pervaiz, E.; Yang, M.; Rabi, O.; Saleem, Z.; Ali, M.; Farrukh, S. A review on nickel cobalt sulphide and their hybrids: Earth abundant, pH stable electro-catalyst for hydrogen evolution reaction. *Int. J. Hydrogen Energy* **2020**, *45*, 24518–24543.
- (43) Dong, D.; Wu, Z.; Wang, J.; Fu, G.; Tang, Y. Recent progress in Co₉S₈-based materials for hydrogen and oxygen electrocatalysis. *J. Mater. Chem. A* **2019**, *7*, 16068–16088.
- (44) Zhang, S.; Zhai, D.; Sun, T.; Han, A.; Zhai, Y.; Cheong, W.-C.; Liu, Y.; Su, C.; Wang, D.; Li, Y. In situ embedding Co₉S₈ into nitrogen and sulfur codoped hollow porous carbon as a bifunctional electrocatalyst for oxygen reduction and hydrogen evolution reactions. *Appl. Catal., B* **2019**, *254*, 186–193.
- (45) Dai, X.; Du, K.; Li, Z.; Liu, M.; Ma, Y.; Sun, H.; Zhang, X.; Yang, Y. Co-Doped MoS₂ Nanosheets with the Dominant CoMoS Phase Coated on Carbon as an Excellent Electrocatalyst for Hydrogen Evolution. *ACS Appl. Mater. Interfaces* **2015**, *7*, 27242–27253.
- (46) Hou, J.; Zhang, B.; Li, Z.; Cao, S.; Sun, Y.; Wu, Y.; Gao, Z.; Sun, L. Vertically Aligned Oxygenated-CoS₂-MoS₂ Heteronanosheet Architecture from Polyoxometalate for Efficient and Stable Overall Water Splitting. *ACS Catal.* **2018**, *8*, 4612–4621.
- (47) Ray, C.; Lee, S. C.; Sankar, K. V.; Jin, B.; Lee, J.; Park, J. H.; Jun, S. C. Amorphous Phosphorus-Incorporated Cobalt Molybdenum Sulfide on Carbon Cloth: An Efficient and Stable Electrocatalyst for Enhanced Overall Water Splitting over Entire pH Values. *ACS Appl. Mater. Interfaces* **2017**, *9*, 37739–37749.
- (48) Zhu, H.; Zhang, J.; Yanzhang, R.; Du, M.; Wang, Q.; Gao, G.; Wu, J.; Wu, G.; Zhang, M.; Liu, B.; Yao, J.; Zhang, X. When Cubic Cobalt Sulfide Meets Layered Molybdenum Disulfide: A Core-Shell System Toward Synergetic Electrocatalytic Water Splitting. *Adv. Mater.* **2015**, *27*, 4752–4759.
- (49) Jin, L.; Lv, C.; Wang, J.; Xia, H.; Zhao, Y.; Huang, Z. Co₉S₈ Nanotubes as an Efficient Catalyst for Hydrogen Evolution Reaction in Alkaline Electrolyte. *Am. J. Anal. Chem.* **2016**, *07*, 210.
- (50) Scherrer, P. Bestimmung der Grosse und der Inneren Struktur von Kolloidteilchen Mittels Rontgenstrahlen. *Math.-Phys. Kl.* **1918**, *2*, 387.
- (51) Mujtaba, J.; Sun, H.; Huang, G.; Zhao, Y.; Arandiyani, H.; Sun, G.; Xu, S.; Zhu, J. Co₉S₈ nanoparticles encapsulated in nitrogen-doped mesoporous carbon networks with improved lithium storage properties. *RSC Adv.* **2016**, *6*, 31775–31781.
- (52) Wang, H.; Lu, S.; Chen, Y.; Han, L.; Zhou, J.; Wu, X.; Qin, W. Graphene/Co₉S₈ nanocomposite paper as a binder-free and free-standing anode for lithium-ion batteries. *J. Mater. Chem. A* **2015**, *3*, 23677–23683.
- (53) Yin, P.-F.; Sun, L.-L.; Gao, Y.-L.; Wang, S.-Y. Preparation and characterization of Co₉S₈ nanocrystalline and nanorods. *Bull. Mater. Sci.* **2008**, *31*, 593–596.
- (54) Feng, L.-L.; Li, G.-D.; Liu, Y.; Wu, Y.; Chen, H.; Wang, Y.; Zou, Y.-C.; Wang, D.; Zou, X. Carbon-Armored Co₉S₈ Nanoparticles as All-pH Efficient and Durable H₂-Evolving Electrocatalysts. *ACS Appl. Mater. Interfaces* **2015**, *7*, 980–988.
- (55) Yin, M.; Feng, X.; Zhao, D.; Zhao, Y.; Li, H.; Zhou, W.; Liu, H.; Bai, X.; Wang, H.; Feng, C.; Jiao, Q. Hierarchical Co₉S₈@Carbon Hollow Microspheres as an Anode for Sodium Ion Batteries with Ultralong Cycling Stability. *ACS Sustainable Chem. Eng.* **2019**, *7*, 6122–6130.
- (56) Zhang, Y.; Wang, N.; Xue, P.; Liu, Y.; Tang, B.; Bai, Z.; Dou, S. Co₉S₈@carbon nanospheres as high-performance anodes for sodium ion battery. *Chem. Eng. J.* **2018**, *343*, 512–519.
- (57) Zeng, P.; Li, J.; Ye, M.; Zhuo, K.; Fang, Z. In Situ Formation of Co₉S₈/N-C Hollow Nanospheres by Pyrolysis and Sulfurization of ZIF-67 for High-Performance Lithium-Ion Batteries. *Chem. – Eur. J.* **2017**, *23*, 9517–9524.
- (58) Jin, R.; Zhou, J.; Guan, Y.; Liu, H.; Chen, G. Mesocrystal Co₉S₈ hollow sphere anodes for high performance lithium ion batteries. *J. Mater. Chem. A* **2014**, *2*, 13241–13244.
- (59) Li, J.; Zheng, G. One-Dimensional Earth-Abundant Nanomaterials for Water-Splitting Electrocatalysts. *Adv. Sci.* **2016**, *4*, 1600380.
- (60) Jiang, P.; Liu, Q.; Ge, C.; Cui, W.; Pu, Z.; Asiri, A. M.; Sun, X. CoP nanostructures with different morphologies: synthesis, characterization and a study of their electrocatalytic performance toward the hydrogen evolution reaction. *J. Mater. Chem. A* **2014**, *2*, 14634–14640.
- (61) Wang, Y.; Zhu, T.; Zhang, Y.; Kong, X.; Liang, S.; Cao, G.; Pan, A. Rational design of multi-shelled CoO/Co₉S₈ hollow microspheres for high-performance hybrid supercapacitors. *J. Mater. Chem. A* **2017**, *5*, 18448–18456.
- (62) Cai, P.; Huang, J.; Chen, J.; Wen, Z. Oxygen-Containing Amorphous Cobalt Sulfide Porous Nanocubes as High-Activity Electrocatalysts for the Oxygen Evolution Reaction in an Alkaline/Neutral Medium. *Angew. Chem., Int. Ed.* **2017**, *56*, 4858–4861.
- (63) Guo, Q.; Ma, Y.; Chen, T.; Xia, Q.; Yang, M.; Xia, H.; Yu, Y. Cobalt Sulfide Quantum Dot Embedded N/S-Doped Carbon Nanosheets with Superior Reversibility and Rate Capability for Sodium-Ion Batteries. *ACS Nano* **2016**, *11*, 12658–12667.
- (64) Ganesan, P.; Prabu, M.; Sanetuntikul, J.; Shanmugam, S. Cobalt Sulfide Nanoparticles Grown on Nitrogen and Sulfur Codoped Graphene Oxide: An Efficient Electrocatalyst for Oxygen Reduction and Evolution Reactions. *ACS Catal.* **2015**, *5*, 3625–3637.
- (65) Zhang, B.-X.; Gao, H.; Li, X.-L. Synthesis and optical properties of nitrogen and sulfur co-doped graphene quantum dots. *New J. Chem.* **2014**, *38*, 4615–4621.
- (66) Wang, Z.; Pan, L.; Hu, H.; Zhao, S. Co₉S₈ nanotubes synthesized on the basis of nanoscale Kirkendall effect and their magnetic and electrochemical properties. *CrystEngComm* **2010**, *12*, 1899–1904.
- (67) Xiao, Y.; Hwang, J.-Y.; Belharouak, I.; Sun, Y.-K. Superior Li/Na-storage capability of a carbon-free hierarchical Co_x hollow nanostructure. *Nano Energy* **2017**, *32*, 320–328.

(68) Shen, M.; Ruan, C.; Chen, Y.; Jiang, C.; Ai, K.; Lu, L. Covalent Entrapment of Cobalt–Iron Sulfides in N-Doped Mesoporous Carbon: Extraordinary Bifunctional Electrocatalysts for Oxygen Reduction and Evolution Reactions. *ACS Appl. Mater. Interfaces* **2015**, *7*, 1207–1218.

(69) Zhou, L.; Zhang, K.; Sheng, J.; An, Q.; Tao, Z.; Kang, Y.-M.; Chen, J.; Mai, L. Structural and chemical synergistic effect of CoS nanoparticles and porous carbon nanorods for high-performance sodium storage. *Nano Energy* **2017**, *35*, 281–289.

(70) Lai, L.; Potts, J. R.; Zhan, D.; Wang, L.; Poh, C. K.; Tang, C.; Gong, H.; Shen, Z.; Lin, J.; Ruoff, R. S. Exploration of the active center structure of nitrogen-doped graphene-based catalysts for oxygen reduction reaction. *Energy Environ. Sci.* **2012**, *5*, 7936–7942.

(71) Guo, D.; Shibuya, R.; Akiba, C.; Saji, S.; Kondo, T.; Nakamura, J. Active sites of nitrogen-doped carbon materials for oxygen reduction reaction clarified using model catalysts. *Science* **2016**, *351*, 361–365.

(72) Fang, G.; Zhou, J.; Cai, Y.; Liu, S.; Tan, X.; Pan, A.; Liang, S. Metal–organic framework-templated two-dimensional hybrid bimetallic metal oxides with enhanced lithium/sodium storage capability. *J. Mater. Chem. A* **2017**, *5*, 13983–13993.

(73) Xu, Y.; Zhou, M.; Wang, X.; Wang, C.; Liang, L.; Grote, F.; Wu, M.; Mi, Y.; Lei, Y. Enhancement of Sodium Ion Battery Performance Enabled by Oxygen Vacancies. *Angew. Chem., Int. Ed.* **2015**, *54*, 8768–8771.

(74) Xie, K.; Wu, H.; Meng, Y.; Lu, K.; Wei, Z.; Zhang, Z. Poly(3,4-dinitrothiophene)/SWCNT composite as a low overpotential hydrogen evolution metal-free catalyst. *J. Mater. Chem. A* **2015**, *3*, 78–82.

(75) Guo, C. X.; Zhang, L. Y.; Miao, J.; Zhang, J.; Li, C. M. DNA-Functionalized Graphene to Guide Growth of Highly Active Pd Nanocrystals as Efficient Electrocatalyst for Direct Formic Acid Fuel Cells. *Adv. Energy Mater.* **2013**, *3*, 167–171.